Research
A SCIENCE PARTNER JOURNAL

RESEARCH ARTICLE

# Synergistic Solvation Strategy for Low-Temperature Alkaline Zinc–Ferricyanide Flow Battery

**Yalu Xin[1], Chen Li[1], Wei Gao[1*], and Yongping Chen[1,2*]**

[1]Key Laboratory of Energy Thermal Conversion and Control of Ministry of Education, School of Energy and Environment, Southeast University, Nanjing, Jiangsu 210096, P. R. China. [2]Jiangsu Key Laboratory of Micro and Nano Heat Fluid Flow Technology and Energy Application, School of Environmental Science and Engineering, Suzhou University of Science and Technology, Suzhou, Jiangsu 215009, P. R. China.

*Address correspondence to: weigao@seu.edu.cn (W.G.); ypchen@seu.edu.cn (Y.C.)

**Citation:** Xin Y, Li C, Gao W, Chen Y. Synergistic Solvation Strategy for Low-Temperature Alkaline Zinc–Ferricyanide Flow Battery. *Research* 2026;9:Article 1118. https://doi.org/10.34133/research.1118

Submitted 21 October 2025
Revised 18 December 2025
Accepted 7 January 2026
Published 2 February 2026

Copyright © 2026 Yalu Xin et al. Exclusive licensee Science and Technology Review Publishing House. No claim to original U.S. Government Works. Distributed under a Creative Commons Attribution License (CC BY 4.0).

Alkaline zinc–ferricyanide flow batteries (AZFFBs) emerge as promising candidates for long-duration energy storage. However, at cryogenic temperatures, these systems suffer from electrolyte solidification, anodic zinc dendrite formation, zinc-related side reactions, and cathodic $Fe(CN)_6^{4-}$ precipitation-induced capacity decay. Herein, we propose a synergistic solvation strategy in which $Li^+$ and $Cl^-$ jointly inhibit the formation of tetrahedral hydrogen bond networks, thereby lowering the liquid–solid transition peak temperature of both the anolyte and catholyte. Meanwhile, $Cl^-$ is utilized to construct a water-poor solvation structure around $Zn(OH)_4^{2-}$ to optimize zinc deposition and inhibit the side reactions, while $Li^+$ enhances the solubility of $Fe(CN)_6^{4-}$ by incorporating additional water molecules into its solvation structure through strong ion–dipole interactions. The optimized AZFFB exhibits outstanding low-temperature performance, achieving stable cycling at −20 °C with an average coulombic efficiency of 99.54%. It also demonstrates excellent stability at room temperature, sustaining over 500 cycles at 28 °C with an average coulombic efficiency of 99.79%, representing more than a 22-fold extension in cycle life. Additionally, the AZFFB exhibits robust stability under fluctuating temperature conditions. These breakthroughs markedly enhance the potential of AZFFBs as viable solutions for extreme-environment energy storage, particularly in polar region microgrids, cold-climate off-grid power systems, and subsea power applications.

## Introduction

The growing need for long-duration energy storage has become increasingly apparent due to the intermittency of renewable energy sources, such as solar and wind power, and the resulting demand for enhanced power system stability and reliability [1–3]. Aqueous redox flow batteries offer a promising solution for long-duration energy storage by providing high efficiency, extended lifespan, exceptional safety, and the advantage of power/capacity decoupling [4–14]. Among these, alkaline zinc–ferricyanide flow batteries (AZFFBs) stand out as optimal candidates for large-scale applications owing to their high electrochemical activity, favorable kinetics, and low cost [15–20]. To enhance the cycling stability of the system, substantial efforts have focused on mitigating zinc dendrite growth and suppressing active-species crossover [21–23]. Strategies to increase ferricyanide solubility have also been widely explored to expand the practical capacity [24–26]. However, these strategies alone are insufficient to ensure robust operation across a broad range of operating conditions. Among them, electrolyte freezing and ferricyanide precipitation at low temperatures markedly constrain the operational range and cycling stability of the system [27–29]. These challenges hinder their deployment in extreme environments such as polar regions, off-grid cold-climate systems, and deep-sea applications, highlighting the urgent need for innovative strategies to develop AZFFBs capable of functioning at low temperatures.

At low temperatures, AZFFBs experience increased hydrogen bonding (HB) among water molecules in the electrolyte, transitioning from initially disordered small water clusters to long-range-ordered HB networks, which ultimately leads to electrolyte freezing [30–32]. To address this, researchers have explored various strategies, including incorporating organic cosolvents, adding chemical additives, and leveraging ion effects, to reconstruct the large HB network, inhibit the formation of ordered tetrahedral structures, and markedly lower the liquid–solid transition peak temperature ($T_t$) of the electrolyte [31,33–36]. Among these approaches, organic antifreeze additives can effectively lower the freezing point, but their high cost, poor chemical stability, and strong interfacial adsorption that occupies electroactive sites and hinders $Zn^{2+}$ transport often limit their practical application [37–39]. Despite these efforts, achieving a low $T_t$ alone is insufficient to ensure stable and efficient AZFFB operation at low temperatures. On

the one hand, low temperatures exacerbate the nonuniform diffusion of ions in the electrolyte, resulting in uneven zinc deposition on the anode [34,40–42]. On the other hand, weakened ion–dipole interactions between $Fe(CN)_6^{4-}$ and water molecules, coupled with enhanced HB among water molecules, reduce the solubility of $Fe(CN)_6^{4-}$, leading to its precipitation and potential channel blockage [43,44]. Unfortunately, few studies have successfully achieved simultaneous reduction of $T_t$, mitigation of zinc-related side reactions, and suppression of cathodic $Fe(CN)_6^{4-}$ precipitation. Reconciling these factors to enable high-performance AZFFBs to operate stably under low-temperature conditions remains an important challenge.

To tackle this issue, we present a synergistic solvation strategy that simultaneously enhances the antifreezing performance of both the anolyte and catholyte, enabling stable operation at temperatures as low as −20 °C, the lowest temperature reported for AZFFBs to date. This strategy applies the polar ions $Li^+$ and $Cl^-$ to effectively disrupt tetrahedral HB networks among water molecules, thereby lowering $T_t$ while simultaneously modifying the solvation structures of $Zn(OH)_4^{2-}$ and $Fe(CN)_6^{4-}$ (Fig. 1). On the anode side, $Cl^-$ strongly interacts with $Zn(OH)_4^{2-}$, partially replacing water molecules in its solvation shell and constructing a water-poor solvation structure to optimize zinc deposition and inhibit side reactions. On the cathode side, the small ionic radius of $Li^+$ allows it to partially replace $K^+$ around $Fe(CN)_6^{4-}$, strengthening ion–dipole interactions and incorporating additional water molecules into its solvation structure, thereby markedly enhancing solubility at low temperatures. As a result, the LiCl-containing AZFFB exhibits remarkably low-temperature performance, maintaining stable operation at −20 °C for 150 cycles at a current density of 20 mA $cm^{-2}$ with average coulombic efficiency (CE) and energy efficiency (EE) values of 99.54% and 74.87%, respectively. Notably, it also demonstrates excellent stability at 28 °C, achieving 500 cycles at a current density of 40 mA $cm^{-2}$ with average CE of 99.79% and EE of 86.84%.

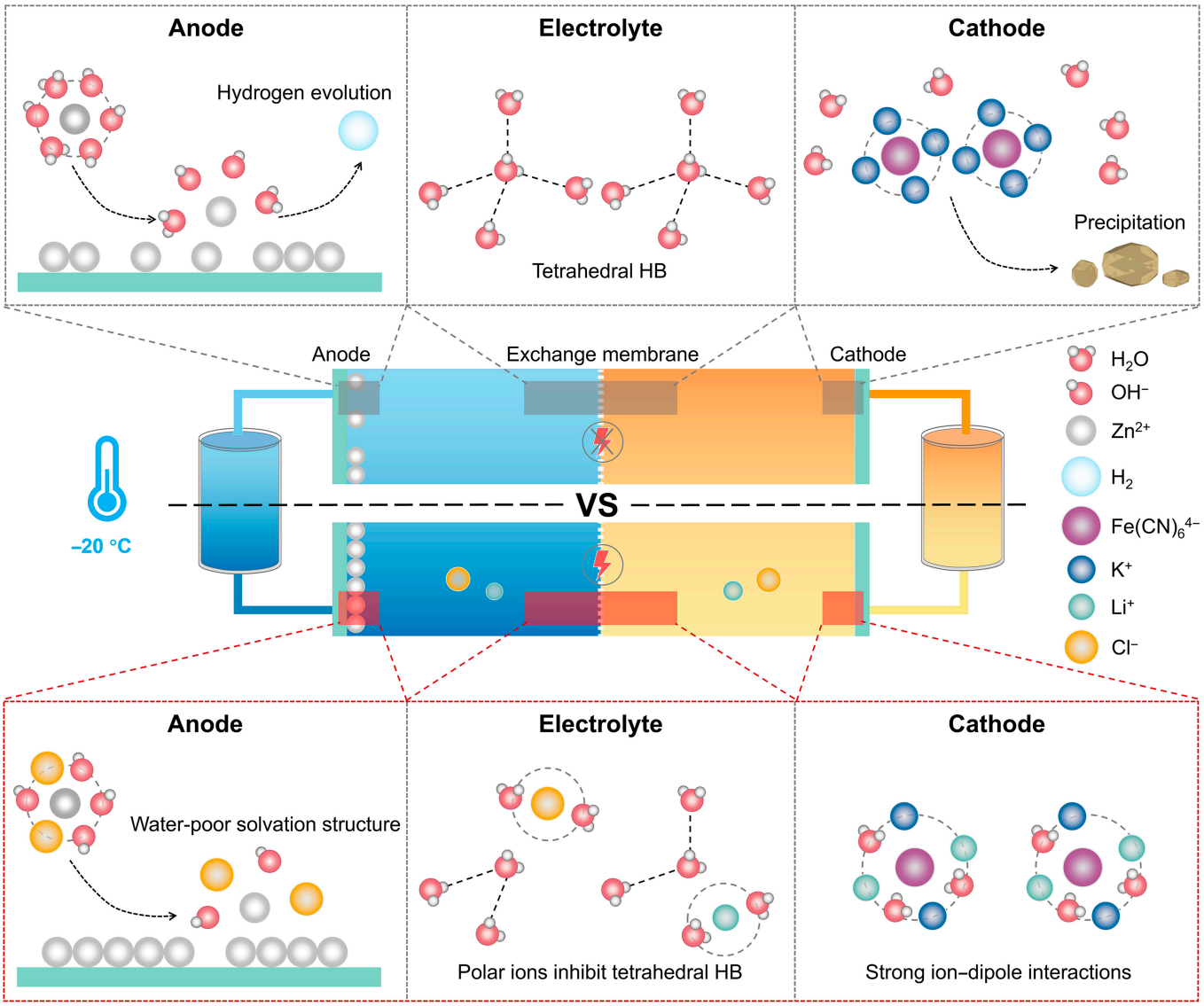



**Fig. 1.** Schematic illustration of the synergistic solvation strategy for alkaline zinc–ferricyanide flow batteries (AZFFBs). The strategy aims to simultaneously reduce $T_t$, optimize zinc deposition, inhibit zinc-related side reactions, and suppress cathodic $Fe(CN)_6^{4-}$ precipitation. HB, hydrogen bonding.

## Results and Discussion

### Design of the synergistic solvation strategy

To overcome the persistent challenges of electrolyte freezing, anode side reactions, and cathode active material precipitation in AZFFBs under low temperatures, this study developed a synergistic solvation strategy that addresses key processes, including HB network reconstruction, $Zn(OH)_4^{2-}$ solvation structure modulation, and enhanced dissolution of $Fe(CN)_6^{4-}$. This strategy employs a $Li^+/Cl^-$ dual-ion synergistic design to engineer polar-ion-mediated HB reconstruction, thereby achieving concurrent electrolyte stabilization and interfacial side reaction inhibition while demonstrating unprecedented cyclability at −20 °C (Fig. 1).

Visualization and differential scanning calorimetry (DSC) were employed to elucidate the effects of $Li^+$ and $Cl^-$ concentrations on the low-temperature stability of alkaline zinc–ferricyanide electrolytes. At −20 °C, optical images clearly reveal that LiCl-containing electrolytes remain unfrozen, whereas the pristine catholyte and anolyte without LiCl undergo visible freezing (Fig. 2A and B). This macroscopic observation indicates that the addition of LiCl markedly improves the low-temperature stability of the electrolytes. DSC measurements provide further insight: The incorporation of $Li^+$ and $Cl^-$ ions markedly reduces $T_t$. When the LiCl concentration reaches 15.5 wt%, the $T_t$ values during freezing decrease to −27.26 and −34.54 °C for the catholyte and anolyte, respectively (Fig. 2C and D and Figs. S1 and S2). Extended measurements confirm that, if necessary, subzero stability can be achieved by increasing the LiCl concentration to achieve even lower $T_t$ values, particularly for the anolyte (Fig. S3). Moreover, optical images demonstrate that higher LiCl concentrations further reduce the $T_t$ of both the catholyte and anolyte, consistent with DSC measurements, while temperature reduction induces $Fe(CN)_6^{4-}$ to precipitate in a LiCl-free catholyte, whereas LiCl-containing electrolytes effectively suppress such precipitation even at low temperatures (Figs. S4 and S5). It is worth noting that although the DSC results show only a small difference in catholyte $T_t$ between 10 and 15.5 wt% LiCl, the freezing behaviors differ markedly under practical operating conditions. In a real flow battery, the large volumes of flowing electrolytes and abundant heterogeneous interfaces promote ice nucleation [45,46]. Consequently, the 10 wt% catholyte freezes at −20 °C, whereas the 15.5 wt% catholyte remains fully liquid and supports stable cycling. In addition, DSC measurements indicate that while the anolyte achieves a $T_t$ comparable to that of the 15.5 wt% LiCl catholyte at a lower concentration of around 12 wt%, the catholyte requires 15.5 wt% to remain stable (Fig. S6). To avoid persistent concentration gradients and disrupt osmotic and compositional balance, 15.5 wt% was adopted for both electrolytes.

The $Li^+$ and $Cl^-$ effectively decrease $T_t$, suppress crystallization, and stabilize $Fe(CN)_6^{4-}$ dissolution in a cryogenic environment, which is attributed to polar-ion-mediated HB reconstruction. To probe the roles of $Li^+$ and $Cl^-$ in modifying solvation structures, $^1$H nuclear magnetic resonance (NMR) spectra were analyzed. The $^1$H NMR spectra demonstrate that adding $Li^+$ and $Cl^-$ causes the chemical shifts of both catholyte and anolyte toward higher fields, indicating an increased electron cloud density around H atoms in water molecules (Fig. 2E). Mechanistically, $Li^+$ interacts with the negatively charged O atoms of water molecules, reducing the electron cloud density around adjacent H atoms, thereby shifting their chemical shifts to a lower field. Conversely, $Cl^-$ binds to the positively charged H atoms, enhancing the electron cloud density around H atoms, which causes the chemical shift to move to higher fields. The stronger ion–dipole interaction between $Cl^-$ and water molecules compared to that of $Li^+$ ultimately dominates the overall upfield shift, resulting in a net increase in hydrogen electron density [47,48]. The ion–dipole interactions between polar ions ($Li^+$ and $Cl^-$) and water molecules disrupt the tetrahedral HB arrangement, thereby elevating configurational entropy. This entropy-driven disorder suppresses the formation of ordered icelike structures, which underlie the cryoprotective functionality of the electrolyte.

The $^{13}$C NMR spectra demonstrate that the chemical shift moves toward a higher field after adding LiCl into the catholyte, reflecting an increased electron cloud density around the C atom (Fig. 2F). This finding suggests that the presence of $Li^+$ inhibits the ionic interaction between $K^+$ and $Fe(CN)_6^{4-}$. The $^7$Li NMR spectra demonstrate that the chemical shift moves toward a higher field after adding the catholyte to the LiCl solution, indicating an increased electron cloud density around $Li^+$ (Fig. 2G). This result implies that $Li^+$ integrates into the solvation structure of $Fe(CN)_6^{4-}$ and partially replaces $K^+$, thereby strengthening the ion–dipole interactions between $Fe(CN)_6^{4-}$ and water molecules. These enhanced interactions facilitate the incorporation of additional water molecules into the solvation structure of $Fe(CN)_6^{4-}$, effectively preventing its aggregation and markedly improving its low-temperature solubility.

To elucidate the synergistic effect of $Li^+$ and $Cl^-$ on the HB configuration of water molecules, $^1$H diffusion-ordered spectroscopy (DOSY) measurements were performed on LiOH and NaCl aqueous solutions, which contain different anions and cations, respectively, in comparison with LiCl. At identical ion concentrations (1 M), the LiCl solution exhibited the lowest diffusion coefficient ($1.83 \times 10^{-9}$ $m^2$ $s^{-1}$) of water molecules, in contrast to the higher values observed for NaCl and LiOH solutions (Fig. 2H to J). The DSC measurements of the 3 aqueous solutions further corroborate that the synergistic interaction between $Li^+$ and $Cl^-$ enables a substantially lower $T_t$ compared with those of LiOH and NaCl aqueous solutions (Fig. S7). This highlights the cooperative effect of $Li^+$ and $Cl^-$ in restructuring the HB network, enabling more effective suppression of tetrahedral configurations under low-temperature conditions.

### Effective reconstruction of the solvation structure

To gain deeper insight into the mechanism by which LiCl enhances the low-temperature stability of alkaline zinc–ferricyanide electrolytes, the solvation structures of the catholyte and anolyte were systematically investigated.

Fourier transform infrared spectroscopy (FTIR) and Raman spectra were performed on the catholyte and anolyte to verify the influence of $Li^+$ and $Cl^-$ on the HB configuration of the water molecule. The results show that $Li^+$ and $Cl^-$ cause a shift in water peaks in both FTIR and Raman spectra (Figs. S8 to S11). To better analyze the impact of water peak shifts on antifreeze performance, the water peaks obtained from FTIR were categorized into 3 subpeaks based on different HB configurations: $\nu_s$ OH, $\nu_{as}$ OH, and $H^f$–O–$H^b$ stretching peaks (Fig. 3A to D). The $\nu_s$ OH stretching peak appears around 3,250 $cm^{-1}$, representing the HB network of water molecules in a regular tetrahedral configuration. The $\nu_{as}$ OH and $H^f$–O–$H^b$ stretching peaks, centered around 3,400 and 3,600 $cm^{-1}$, respectively,

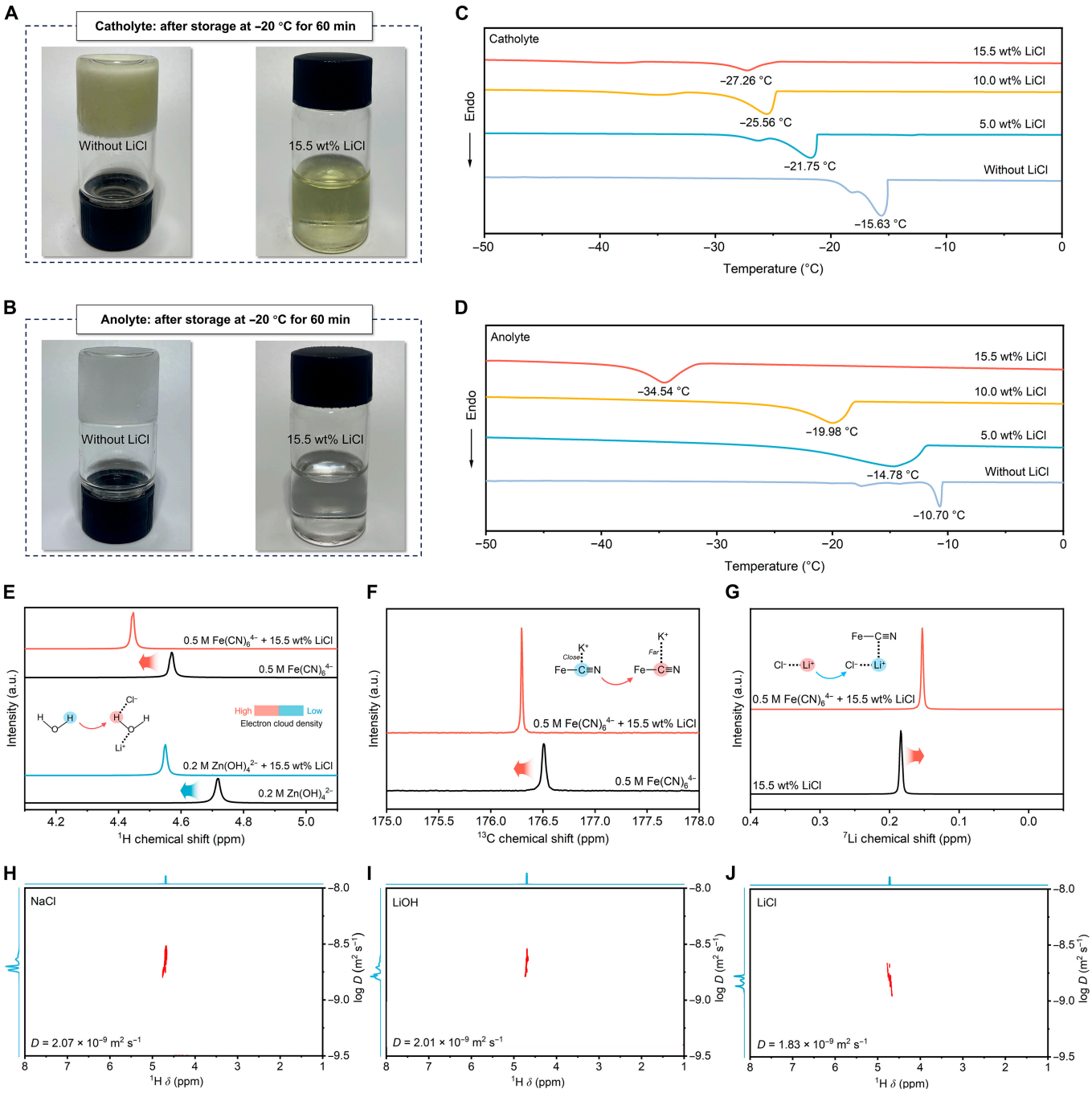



**Fig. 2.** Mechanistic investigation of $Li^+$ and $Cl^-$ enhanced the antifreezing characteristics of AZFFB electrolytes. (A) Optical images of catholytes with and without LiCl at −20 °C. (B) Optical images of anolytes with and without LiCl at −20 °C. (C) The $T_t$ evolution of the catholyte with increasing LiCl concentration. (D) The $T_t$ evolution of the anolyte with increasing LiCl concentration. (E) $^1$H nuclear magnetic resonance (NMR) spectra illustrating the influence of $Li^+$ and $Cl^-$ on the electron cloud density around the H atoms of water molecules. (F) $^{13}$C NMR spectra demonstrating the effect of $Li^+$ on the C≡N chemical shift of $Fe(CN)_6^{4-}$ in the catholyte. (G) $^7$Li NMR spectra evidence for electron cloud density redistribution around $Li^+$ in the catholyte. (H) $^1$H DOSY spectra of water molecules in 1 M NaCl. (I) $^1$H DOSY spectra of water molecules in 1 M LiOH. (J) $^1$H diffusion-ordered spectroscopy (DOSY) spectra of water molecules in 1 M LiCl.

represent the HB network of water molecules with incomplete coordination [31]. A higher proportion of $\nu_{as}$ OH and $H^f$–O–$H^b$ stretching peaks correlates with a lower likelihood that the electrolyte will freeze. The FTIR spectra indicate that the addition of 15.5 wt% LiCl increases the proportion of incompletely coordinated HB in water molecules of the catholyte by 4.57% (Fig. 3A and B) and in the anolyte by 6.93% (Fig. 3C and D).

Adsorption energy analysis reveals that the interaction between $Zn^{2+}$ and $Cl^-$ is markedly stronger than that between $Zn^{2+}$ and $H_2O$, indicating that $Cl^-$ can displace water molecules in the solvation shell of $Zn(OH)_4^{2-}$ (Fig. 3E and Note S1). The adsorption energy of $Fe(CN)_6^{4-}$ with $Li^+$ is much higher than that with $K^+$, while the $Li^+$–$H_2O$ interaction exceeds $K^+$–$H_2O$. This suggests that $Li^+$ not only replaces partial $K^+$ around $Fe(CN)_6^{4-}$ but also enhances the water molecule content in its solvation

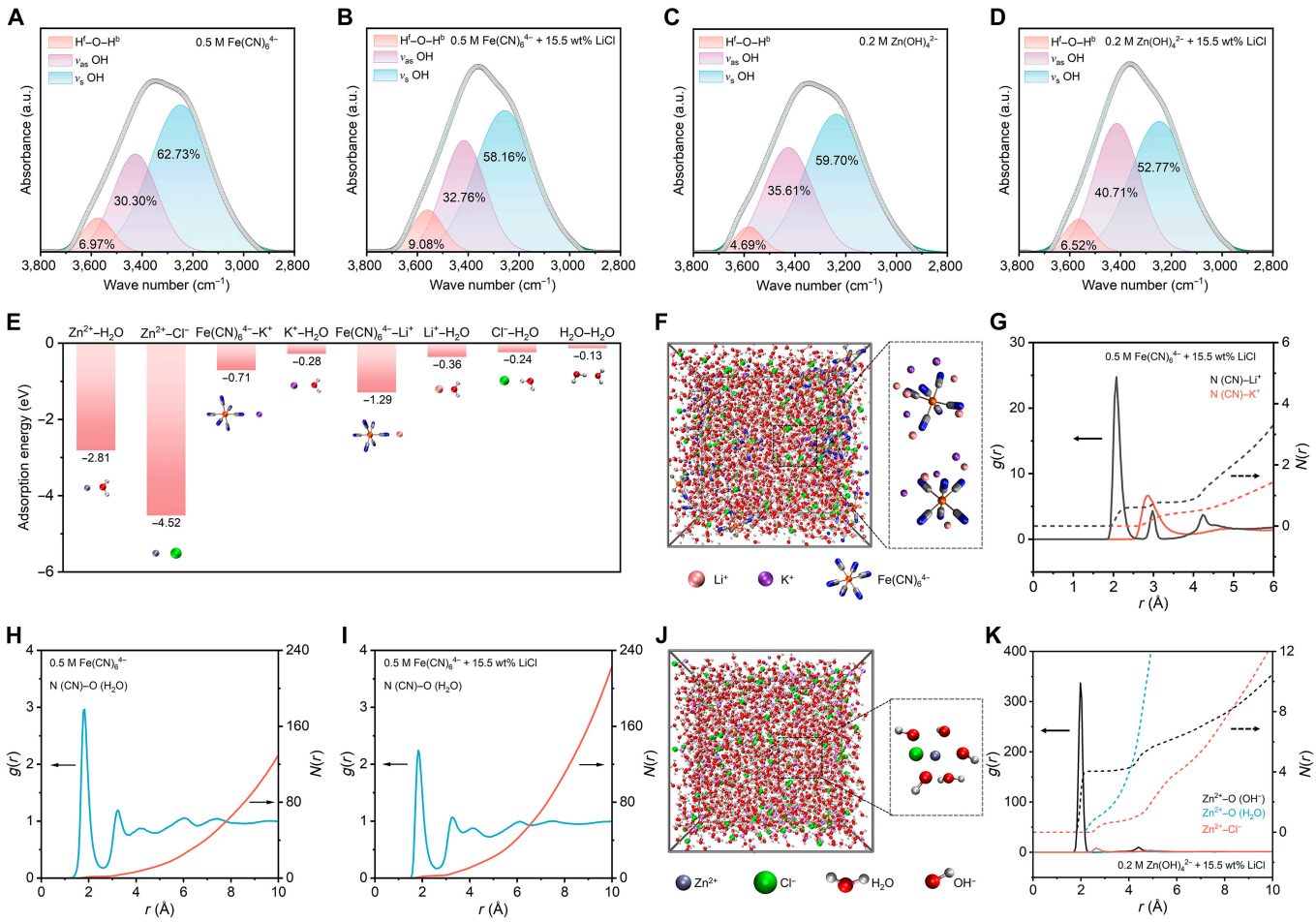



**Fig. 3.** Verification of the effective reconstruction of the solvation structure in the electrolyte of AZFFBs. (A) Proportions of 3 subpeaks in the Fourier transform infrared spectroscopy (FTIR) water spectrum of the catholyte without $Li^+$ and $Cl^-$. (B) Proportions of 3 subpeaks in the FTIR water spectrum of the catholyte with $Li^+$ and $Cl^-$. (C) Proportions of 3 subpeaks in the FTIR water spectrum of the anolyte without $Li^+$ and $Cl^-$. (D) Proportions of 3 subpeaks in the FTIR water spectrum of the anolyte with $Li^+$ and $Cl^-$. (E) Adsorption energies of different substances in the anolyte and catholyte. (F) Molecular dynamics (MD) simulation of the catholyte containing $Li^+$. (G) Radial distribution functions of N (CN)–$Li^+$ and N (CN)–$K^+$ in the catholyte containing $Li^+$. (H) Radial distribution function of N (CN)–O ($H_2O$) in the catholyte without $Li^+$. (I) Radial distribution function of N (CN)–O ($H_2O$) in the catholyte containing $Li^+$. (J) MD simulation of the anolyte containing $Cl^-$. (K) Radial distribution functions of $Zn^{2+}$–O ($OH^-$), $Zn^{2+}$–O ($H_2O$), and $Zn^{2+}$–$Cl^-$ in the anolyte containing $Cl^-$.

shell. Additionally, comparative adsorption energy data confirm that both $Li^+$ and $Cl^-$ inhibit the formation of HB among water molecules. Molecular dynamics simulations elucidate the reconstruction of the solvation structure of $Fe(CN)_6^{4-}$ and $Zn(OH)_4^{2-}$ induced by $Li^+$ and $Cl^-$ (Fig. 3F to K, Table S1, and Note S2). Radial distribution function analysis shows that in the catholyte containing $Li^+$ and $Cl^-$, 3 characteristic $Li^+$ peaks appear at 2.1, 3.0, and 4.2 Å from the N atom (Fig. 3F and G). Within 6 Å of the N atom in $Fe(CN)_6^{4-}$, the average coordination numbers of $K^+$ and $Li^+$ are 1.45 and 3.33, respectively. This suggests that $Li^+$ can be integrated into the solvation structure of $Fe(CN)_6^{4-}$. By comparing the intensities of the N (CN)–$K^+$ characteristic peaks in the presence and absence of LiCl, it is confirmed that $Li^+$ markedly weakens the adsorption strength between $K^+$ and $Fe(CN)_6^{4-}$ (Figs. S12 and S13). Furthermore, radial distribution function analysis of water molecules around the N atom confirms that adding LiCl markedly increases the number of water molecules surrounding $Fe(CN)_6^{4-}$ (Fig. 3H and I and Table S2). Molecular dynamics simulations of the anolyte indicate that $Cl^-$ can replace some water molecules in the solvation structure of $Zn(OH)_4^{2-}$, which helps reduce the number of active water molecules during desolvation, thereby inhibiting the hydrogen evolution reaction (Fig. 3J) [49–51]. Based on radial distribution functions, within 3 Å of $Zn^{2+}$, the average coordination numbers of $OH^-$, $H_2O$, and $Cl^-$ are 4.05, 1.31, and 0.70, respectively (Fig. 3K). These simulation results can strongly support the experimental data.

## Electrochemical stability of electrodes

The synergistic solvation strategy effectively addresses key challenges in the AZFFB by simultaneously reducing $T_t$, improving zinc deposition, mitigating zinc-related side reactions, and suppressing cathodic $Fe(CN)_6^{4-}$ precipitation. This coordinated approach ensures excellent electrochemical stability in both the cathode and anode. The addition of LiCl can markedly optimize zinc deposition, and this effect becomes more pronounced as the temperature decreases (Fig. 4A and B and Figs. S14 to S17). Chronoamperometric (CA) analysis reveals that the zinc deposition behavior varies markedly with LiCl concentration. The electrolyte without LiCl exhibits a low and stable current density corresponding to sluggish 2-dimensional surface-limited nucleation (Fig. 4C). With 5.0 wt% LiCl, the nucleation rate

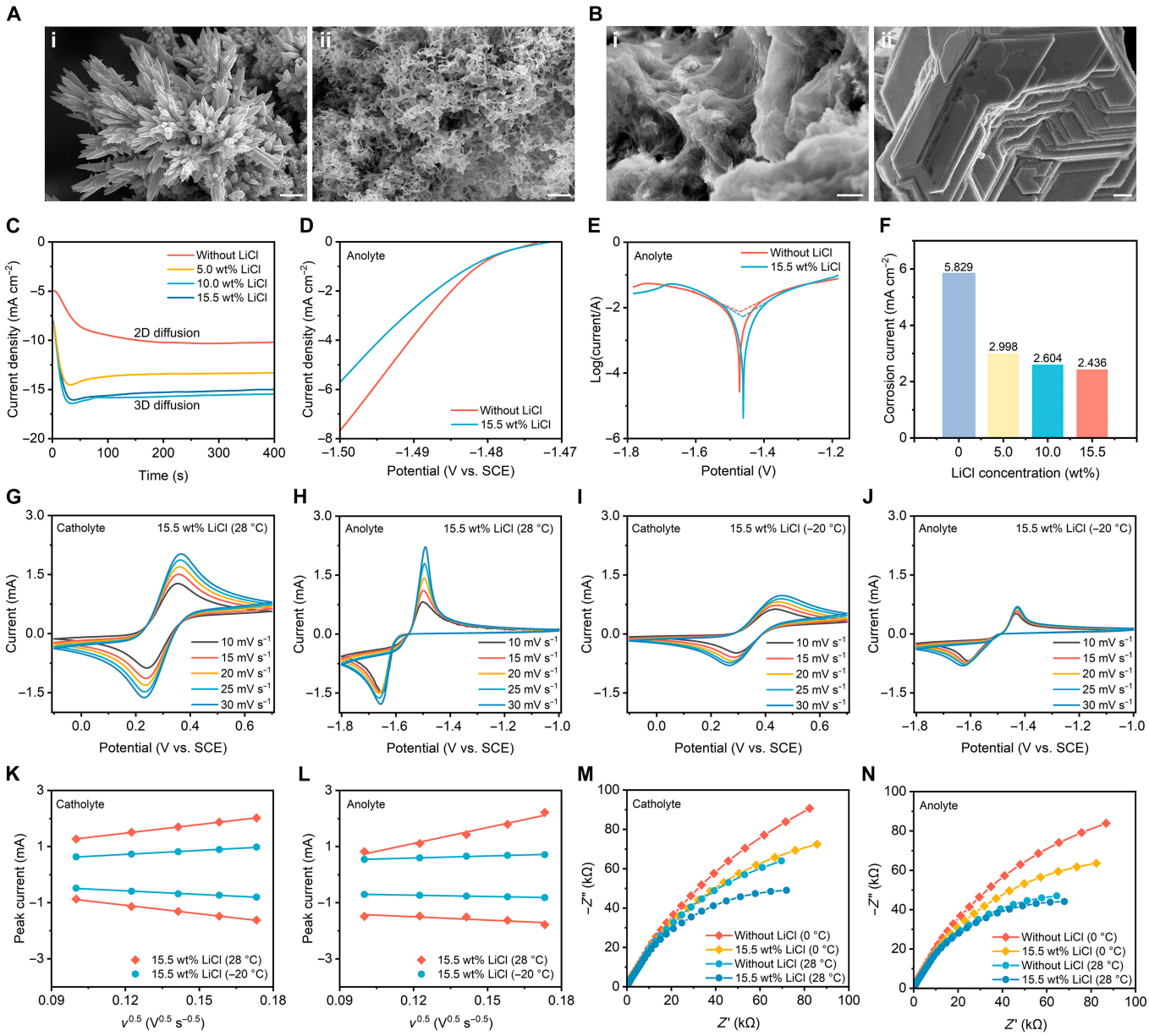



**Fig. 4.** The influence of LiCl on cathode and anode stability. (A) Scanning electron microscopy (SEM) images of zinc deposited on the surface of the graphite felt electrode at 10 mAh $cm^{-2}$ areal capacity and 10 mA $cm^{-2}$ current density in the anolyte without LiCl at 28 and 0 °C. Scale bar: 2 μm. (B) SEM images of zinc deposited on the surface of the graphite felt electrode at 10 mAh $cm^{-2}$ areal capacity and 10 mA $cm^{-2}$ current density in the anolyte with 15.5 wt% LiCl at 28 and 0 °C. Scale bar: 2 μm. (C) Chronoamperometric (CA) curves of the anolyte with increasing LiCl concentrations at a constant overpotential of −150 mV. (D) Linear sweep voltammetry (LSV) curves of the anolyte with and without LiCl. (E) Tafel curves of the anolyte with and without LiCl. (F) The corrosion current evolution of anolyte with increasing LiCl concentration. (G) Cyclic voltammetry (CV) curves of the catholyte at varying scan rates at 28 °C. (H) CV curves of the anolyte at varying scan rates at 28 °C. (I) CV curves of the catholyte at varying scan rates at −20 °C. (J) CV curves of the anolyte at varying scan rates at −20 °C. (K) Linear corrections of the LiCl-containing catholyte at 28 and −20 °C between the peak currents from oxidation and reduction processes and the square root of the scan rate. (L) Linear corrections of the LiCl-containing anolyte at 28 and −20 °C between the peak currents from oxidation and reduction processes and the square root of the scan rate. (M) Electrochemical impedance spectroscopy (EIS) of the catholyte with different LiCl concentrations. (N) EIS of the anolyte with different LiCl concentrations. 2D, 2-dimensional; 3D, 3-dimensional; SCE, saturated calomel electrode.

increases moderately, while further increasing the LiCl concentration to 10.0 and 15.5 wt% results in a higher steady-state current density, indicating a transition to diffusion-controlled 3-dimensional zinc growth. These findings demonstrate that LiCl addition effectively promotes 3-dimensional nucleation and enables more uniform zinc deposition [52]. Even at −20 °C, scanning electron microscopy observations confirm that the presence of LiCl enables uniform and compact zinc deposition, demonstrating its robust interfacial stabilization capability under low-temperature conditions (Fig. S18). Linear sweep voltammetry (LSV) measurements demonstrate that the addition of LiCl suppresses the hydrogen evolution reaction on the anode, with the inhibitory effect increasing linearly with LiCl concentration (Fig. 4D and Fig. S19). Tafel curves further confirm that LiCl addition enhances anodic corrosion resistance, indicating suppressed hydrogen evolution and a more favorable competition toward zinc deposition (Fig. 4E and F and Fig. S20).

The cyclic voltammetry (CV) analysis demonstrates that the introduction of $Li^+$ and $Cl^-$ enables both electrolytes to maintain highly symmetric anodic and cathodic peaks across scan rates of 10 to 30 mV $s^{-1}$ and a wide temperature range from −20 to 28 °C, indicating preserved redox reversibility (Fig. 4G to J). With decreasing temperature, the ion-diffusion rate slows down, causing the peak currents at −20 °C to be markedly reduced, while those at 0 °C fall between the values observed at 28 and −20 °C (Figs. S21 and S22). Meanwhile, quantitative evaluation of the ion-diffusion coefficients reveals the ion transport characteristics under different working conditions (Note S3 and Table S3). At 28 °C, the diffusion coefficients of the catholyte redox couple with LiCl are $9.39 \times 10^{-7}$ and $9.17 \times 10^{-7}$ $cm^2$ $s^{-1}$. Under the same ambient temperature, the diffusion coefficients of the anolyte redox couple with LiCl are $2.50 \times 10^{-6}$ and $1.07 \times 10^{-7}$ $cm^2$ $s^{-1}$. When the ambient temperature decreases to −20 °C, the diffusion coefficients of the catholyte redox couple with the LiCl are $2.44 \times 10^{-7}$ and $2.03 \times 10^{-7}$ $cm^2$ $s^{-1}$, and those of the anolyte redox pairs with the LiCl are $4.96 \times 10^{-8}$ and $2.03 \times 10^{-8}$ $cm^2$ $s^{-1}$ (Fig. 4K and L). The decrease in temperature did not cause a sharp drop in the diffusion coefficients of the electrolytes, suggesting that adding $Li^+$ and $Cl^-$ lowers the electrolyte's $T_t$ and enables it to maintain good electrochemical performance under low-temperature conditions. In addition, the incorporation of $Li^+$ and $Cl^-$ slightly decreases the diffusion coefficients of both the catholyte and anolyte, which can be attributed to the increased electrolyte viscosity caused by the higher salt concentration, thereby enhancing internal friction and hindering ion diffusion (Figs. S23 to S25). Electrochemical impedance spectroscopy (EIS) results show that at 28 °C, adding 15.5 wt% LiCl markedly reduces catholyte impedance, reflecting enhanced ionic conductivity and mitigating interfacial polarization (Fig. 4M and N). At 0 °C, the overall impedance increases markedly due to hindered ion transport. However, LiCl incorporation still alleviates interfacial resistance, underscoring its beneficial effect even under low-temperature conditions.

FTIR analysis was performed on the electrolytes before and after battery cycling and static storage to evaluate the impact of $Li^+$ and $Cl^-$ on the chemical stability of the catholyte and anolyte. The results demonstrate that no structural degradation occurs in either the reduced-state catholyte or the oxidized-state anolyte after 500 charge–discharge cycles (Fig. S26). The sole detectable change is a weak stretching vibration at ~2,040 $cm^{-1}$ in the cycled anolyte, assigned to the C≡N bond vibration of $Fe(CN)_6^{4-}$. This phenomenon originates from the intrinsic ion crossover effect of the Nafion proton-exchange membrane, which allows trace $Fe(CN)_6^{4-}$ migration into the anolyte compartment during operation. In addition, long-term stability tests further confirm the robustness of the electrolyte. When the reduced-state catholyte and oxidized-state anolyte are stored separately for 20 d, FTIR spectra show no compositional changes (Fig. S27). Collectively, these findings validate that LiCl incorporation preserves the chemical stability of both the catholyte and anolyte under operational and storage conditions.

### Long-term cycling performance of AZFFBs at low temperatures

To evaluate the temperature adaptability of the synergistic solvation strategy in AZFFBs, cycling performance tests were conducted at both room temperature (28 °C) and low temperature (−20 °C) using battery configurations with an active area of 13.5 $cm^2$ (Fig. S28 and Note S3). Precise temperature regulation is achieved through an environmental chamber equipped with proportional–integral–derivative control (Fig. S29). At 28 °C and a current density of 40 mA $cm^{-2}$, the LiCl-containing AZFFB exhibits markedly extended cycling stability compared with the rapid failure of the LiCl-free AZFFB (Fig. 5A and Fig. S30). The enlarged voltage profiles in Fig. 5B highlight the severe polarization in the LiCl-free cell, whereas the LiCl-containing cell maintains stable charge–discharge curves. Moreover, as illustrated in Fig. 5C, the voltage profiles of the LiCl-containing cell at the 100th, 300th, and 500th cycles nearly overlap, confirming its excellent long-term stability. Meanwhile, the average CE and EE of the LiCl-containing AZFFB reach 99.79% and 86.84%, respectively, over the first 500 cycles (Fig. 5D). By contrast, the LiCl-free AZFFB undergoes rapid performance decay under 70% state of charge (SOC) conditions, with voltage polarization emerging from the 22nd cycle and average CE and EE values of 97.66% and 75.82% over the first 30 cycles. The incorporation of LiCl remarkably improves the cycling stability of the AZFFB at room temperature, achieving more than a 22-fold enhancement and substantially increasing CE and EE by 2.13% and 11.02%, respectively. These collective results demonstrate that the synergistic solvation strategy enables room-temperature stability.

For low-temperature validation with a current density of 20 mA $cm^{-2}$ and a charging cutoff condition of 70% SOC, the AZFFB completes 150 cycles while maintaining stable charge–discharge voltages, with average CE and EE values of 99.54% and 74.87%, respectively (Fig. 5E and F and Fig. S31). As shown in Fig. 5G, the duration of a single cycle exceeds 1 h. Moreover, the discharge profiles at the 5th, 70th, and 140th cycles nearly overlap, further demonstrating the excellent reversibility and low polarization of the battery even under low-temperature operation (Fig. 5H). These findings indicate that AZFFB exhibits outstanding electrochemical reversibility and stable energy output with negligible capacity fading, confirming its strong potential for reliable long-term operation even under subzero conditions. In conclusion, these results set new performance benchmarks for AZFFBs in both cycling stability and operational temperature range, markedly outperforming existing studies (Fig. 5I and Table S4) [43,44,53–59].

To investigate the impact of thermal stress in practical AZFFB operation, such as extreme weather, diurnal variations, and load switching, specifically programmed thermal cycling tests were conducted on AZFFBs, simulating temperature transitions from −20 to 30 °C (Note S3). The thermal protocol utilizes a 0.5 °C $min^{-1}$ ramp rate between 10 °C intervals with 4-h stabilization at each temperature node. Progressive temperature increases reduce charge/discharge voltages through accelerated redox reaction kinetics, while subsequent cooling phases gradually restore polarization characteristics (Fig. 5J and Figs. S32 and S33). Throughout thermal cycling, the battery maintains a CE of 99.86% and an EE of 86.01% (Fig. 5K), demonstrating complete electrochemical reversibility under thermal stress. This temperature-independent performance confirms the synergetic solvation strategy's viability for field deployment in regions with daily temperature fluctuations exceeding 25 °C, without requiring auxiliary thermal regulation systems.

## Conclusion

In this work, we report a synergistic solvation strategy that enables the stable operation of AZFFBs at a low temperature of −20 °C by introducing ions with strong dipole interactions.

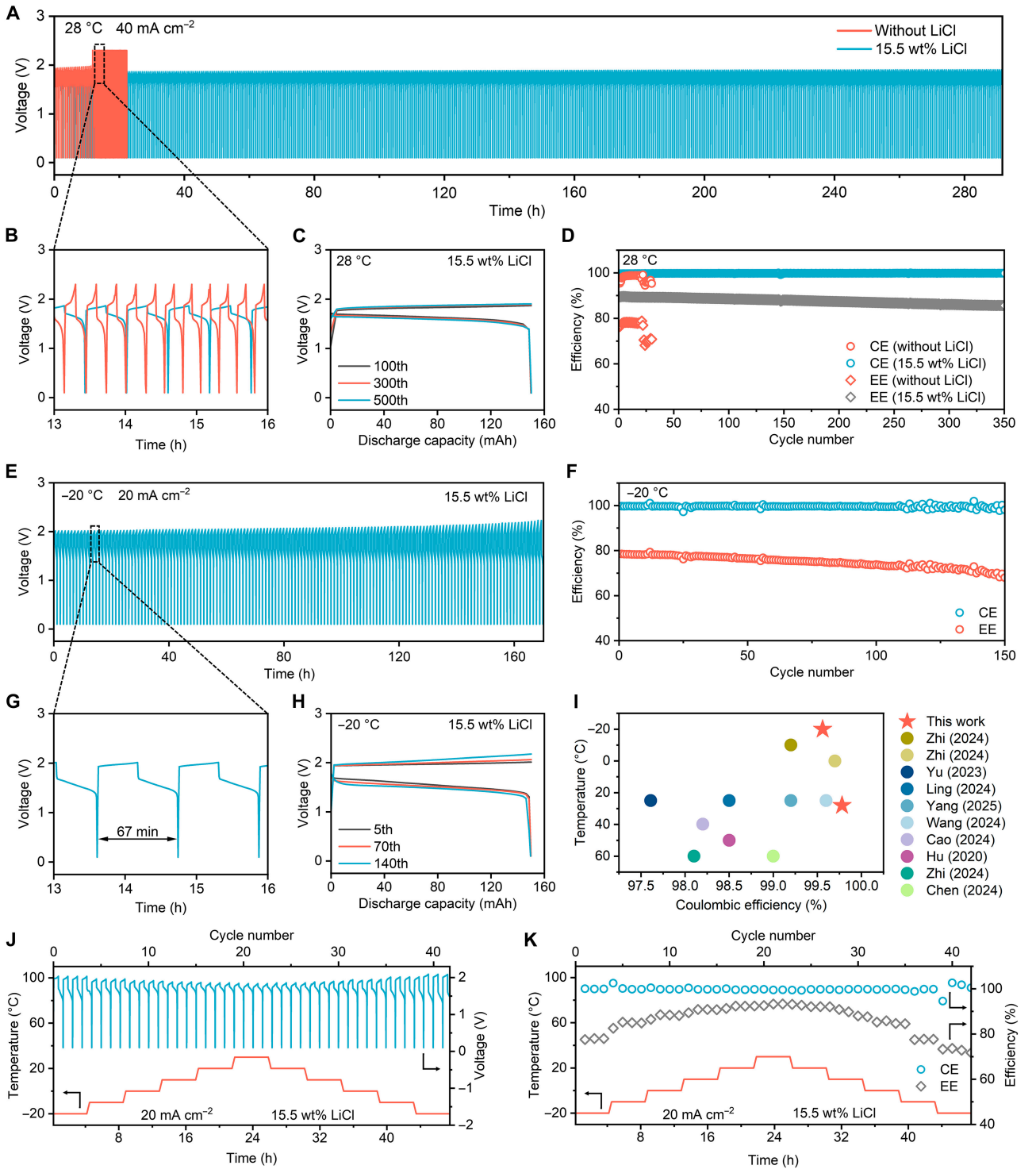



**Fig. 5.** The electrochemical cycling performance of AZFFBs. (A) Voltage curves of the AZFFB during charge–discharge cycling with and without LiCl at 28 °C under a 40 mA $cm^{-2}$ current density. (B) Enlarged view of the voltage curves between 13 and 16 h. (C) Representative voltage curves of the LiCl-containing AZFFB at the 100th, 300th, and 500th cycles. (D) Coulombic efficiency (CE) and energy efficiency (EE) of the AZFFB with and without LiCl at 28 °C under 40 mA $cm^{-2}$ current density. (E) Voltage curves of the LiCl-containing AZFFB during charge–discharge cycling at −20 °C under a 20 mA $cm^{-2}$ current density. (F) CE and EE of the LiCl-containing AZFFB at −20 °C under a 20 mA $cm^{-2}$ current density. (G) Enlarged view of the voltage curves between 13 and 16 h. (H) Representative voltage curves of the LiCl-containing AZFFB at the 5th, 70th, and 140th cycles. (I) Performance comparison of this work with existing research on zinc–ferricyanide flow batteries. (J) Voltage curves of the LiCl-containing AZFFB during charge–discharge cycling under a 20 mA $cm^{-2}$ current density and over a thermal cycling range of −20 to 30 °C. (K) CE and EE evolution of the LiCl-containing AZFFB during −20 to 30 °C thermal cycling under a 20 mA $cm^{-2}$ current density.

We employ the synergistic effect of $Li^+$ and $Cl^-$ to effectively inhibit the formation of tetrahedral hydrogen bond networks while modulating the solvation structures of $Fe(CN)_6^{4-}$ and $Zn(OH)_4^{2-}$. Specifically, on the cathode side, $Li^+$ partially replaces $K^+$ in the solvation structure of $Fe(CN)_6^{4-}$ and incorporates additional water molecules, markedly suppressing

$Fe(CN)_6^{4-}$ precipitation at low temperatures. On the anode side, $Li^+$ disrupts the solvation structure of $Zn(OH)_4^{2-}$, while $Cl^-$ replaces some water molecules within the solvation shell, thereby improving zinc deposition and reducing side reactions. As a result, the optimized AZFFB achieves stable operation at −20 °C with average CE and EE values of 99.54% and 74.87%, respectively. It also demonstrates enhanced cycling stability at room temperature and robust stability under temperature fluctuations. This work provides an effective design strategy for achieving stable performance of redox flow batteries under extreme cold conditions.

## Materials and Methods

### Chemicals and materials

Lithium hydroxide, sodium chloride, sodium hydroxide, and lithium chloride were purchased from Aladdin. Potassium ferrocyanide, potassium ferricyanide, and zinc oxide were purchased from Sigma-Aldrich. The purity of all chemicals and materials reached analytical grade, and they could be directly used in experiments without further purification. The Nafion 115 (Dupont) membrane was purchased from Chemours. All experiments in this work were conducted using deionized water.

### DSC measurements

The phase transition temperature of the electrolyte was measured using a differential scanning calorimeter (DSC8000, Waltham, USA). Firstly, the sample was maintained at 25 °C for 5 min, and then the temperature of the sample was decreased from 25 to −65 °C at a cooling rate of 5 °C $min^{-1}$.

### NMR measurements

NMR analysis of the anolyte and catholyte was conducted using the Bruker Avance III HD 600-MHz spectrometer (Bruker, Germany) to demonstrate the variations of $^1H$, $^7Li$, and $^{13}C$ chemical shifts in various electrolytes at room temperature. A liquid sample was prepared using a coaxial double-tube setup, where the inner tube was loaded with deuterated reagent ($D_2O$) and the outer tube contained the target sample.

### $^1H$ DOSY measurements

$^1H$ DOSY spectra were acquired on a Bruker Avance III HD 600-MHz spectrometer (Bruker, Germany). Electrolyte samples were prepared in deuterated reagent ($D_2O$) and measured at 28 °C.

### FTIR and Raman spectroscopy measurements

At room temperature, the FTIR spectra of the electrolytes were recorded using a Fourier transform infrared spectrometer (Thermo Nicolet iS50, Waltham, USA), and the Raman spectra were obtained with a micro-Raman spectrometer (HORIBA France SAS XploRA, Palaiseau, France). For the FTIR comparison before and after cycling, the post-cycled electrolyte was collected from the AZFFB experiment carried out at 28 °C.

### CA, LSV, Tafel, CV, and EIS measurements

All electrochemical measurements were conducted on an electrochemical workstation (CHI700E, Shanghai, China). CA was performed using a 2-electrode configuration, whereas LSV, Tafel, CV, and EIS measurements were carried out using a 3-electrode configuration.

#### *CA measurements*

A symmetric Zn||Zn cell was employed, in which both electrodes were zinc foils. For the anolyte, the concentration of $Zn(OH)_4^{2-}$ was 0.2 mol $l^{-1}$, and that of NaOH was 2 mol $l^{-1}$. For the anolyte with added LiCl, the concentrations of LiCl were 5.0, 10.0, and 15.5 wt%, respectively. The CA tests were conducted at an overpotential of −150 mV at 28 °C.

#### *LSV and Tafel measurements*

A zinc foil glassy carbon electrode was selected to serve as the working electrode, a saturated calomel electrode was picked as the reference electrode, and a platinum plate electrode was selected as the counter electrode. For the anolyte, the concentration of $Zn(OH)_4^{2-}$ was 0.2 mol $l^{-1}$, and that of NaOH was 2 mol $l^{-1}$. For the anolyte with added LiCl, the concentrations of LiCl were 5.0, 10.0, and 15.5 wt%, respectively. For LSV measurements, the anolyte was tested at a 1 mV $s^{-1}$ scan rate at 28 °C. For Tafel measurements, the anolyte was tested at a 10 mV $s^{-1}$ scan rate at 28 °C.

#### *CV measurements*

A glassy carbon electrode was selected to serve as the working electrode, a saturated calomel electrode was picked as the reference electrode, and a platinum plate electrode was selected as the counter electrode. For the anolyte, the concentration of $Zn(OH)_4^{2-}$ was 0.2 mol $l^{-1}$, and that of NaOH was 2 mol $l^{-1}$. For the catholyte, the concentration of $K_4[Fe(CN)_6]$ was 0.5 mol $l^{-1}$, and that of NaOH was 0.5 mol $l^{-1}$. For the electrolyte with added LiCl, the concentration of LiCl was 15.5 wt%. The anolyte and catholyte were tested at different scan rates (10 to 30 mV $s^{-1}$) at 0 and 28 °C.

#### *EIS measurements*

EIS was carried out with a glassy carbon electrode serving as the working electrode, alongside a saturated calomel electrode as the reference electrode and a platinum plate as the counter electrode. For the anolyte, the $Zn(OH)_4^{2-}$ concentration was 0.2 mol $l^{-1}$, and that of NaOH was 2 mol $l^{-1}$. For the catholyte, the concentration of $K_4[Fe(CN)_6]$ was 0.5 mol $l^{-1}$, and that of NaOH was 0.5 mol $l^{-1}$. For the electrolyte with added LiCl, the concentrations of LiCl were 5.0, 10.0, and 15.5 wt%, respectively. The anolyte and catholyte were measured within the frequency range spanning 0.1 Hz to 100 kHz, with measurements taken at 0 and 28 °C.

### Assembly of the flow battery

The AZFFB experiments were conducted using a battery fixture with an active area of 4.5 × 3 $cm^2$ (LSB-3, Wuhan Zhisheng New Energy Co., Ltd.) and a design without flow channels. All the charge–discharge experiments of the AZFFBs were conducted using graphite felts (thickness: 4.35 mm) as electrodes and Nafion 115 membranes as proton-exchange membranes. To increase the hydrophilicity of the graphite felts, they were heated in a muffle furnace at 500 °C for 2 h before the experiments. A peristaltic pump circulated the electrolyte between the storage tank and the battery fixture, with the electrolyte flow rate set at 50 ml $min^{-1}$. The flow battery was subjected to charge and discharge experiments using the LAND battery test system (CT2001A, Wuhan, China). The NEWARE high–low temperature test chamber (MGDW-408-40, Shenzhen, China) was used to control the ambient temperature.

### *Electrolyte preparation*

The anolyte was prepared from ZnO, NaOH, and deionized water, where the white powdery ZnO was dissolved in NaOH solution under magnetic stirring until complete dissolution. The catholyte was prepared from $K_4[Fe(CN)_6]$, NaOH, and deionized water, with $K_4[Fe(CN)_6]$ fully dissolved in the NaOH solution under magnetic stirring. For the LiCl-containing battery experiments, LiCl was introduced into both the anolyte and catholyte, followed by continuous magnetic stirring until complete dissolution. The concentrations of the redox-active species and NaOH were determined based on the volume of water at room temperature (28 °C), while the amount of LiCl added was calculated relative to the mass of water and was independent of temperature. Considering the marked variation of electrolyte volume with temperature and the nonconstancy of molar concentration at low temperatures, this study employed mass fraction, independent of temperature, to represent the additive content.

### *Testing conditions*

For all AZFFB experiments, the $Zn(OH)_4^{2-}$ in the zinc-based electrolyte was 0.2 mol $l^{-1}$, and the concentration of NaOH was 2 mol $l^{-1}$. The $K_4[Fe(CN)_6]$ concentration was 0.5 mol $l^{-1}$, and the concentration of NaOH was 0.5 mol $l^{-1}$. For the additive-containing battery experiments, the LiCl content was 15.5 wt%. The anolyte and catholyte volumes were fixed at 20 ml, with charging terminated upon reaching either 70% SOC in the anolyte or a cutoff voltage of 2.3 V, and discharging stopped at 0.1 V. A current density of 40 mA $cm^{-2}$ was applied at 28 °C, while a current density of 20 mA $cm^{-2}$ was used at −20 °C and under variable-temperature operation. The adopted SOC and corresponding areal capacity fall within the ranges widely reported for AZFFBs, ensuring reversible zinc plating/stripping and reliable performance evaluation [23,26,43,44,54,59,60].

## Acknowledgments

**Funding:** This work was supported by the National Natural Science Foundation of China (Grant Nos. 52476061, 52036006, 92271111, and 52022020), the Joint Foundation of Ministry of Education and Equipment Pre-research of China (Grant No. 8091B022125), and the Start-up Research Fund of Southeast University (Grant No. RF1028623301).

**Author contributions:** Y.X.: Investigation, methodology, visualization, writing—original draft, and data curation. C.L.: Writing—original draft. W.G.: Methodology, writing—review and editing, supervision, funding acquisition, and conceptualization. Y.C.: Validation, writing—review and editing, supervision, funding acquisition, and conceptualization.

**Competing interests:** The authors declare that they have no competing interests.

## Data Availability

The data supporting this article are included as part of the Supplementary Materials.

## Supplementary Materials

Figs. S1 to S33
Tables S1 to S4
Notes S1 to S3

## References

1. Chu S, Cui Y, Liu N. The path towards sustainable energy. *Nat Mater*. 2016;16(1):16–22.
2. Chu S, Majumdar A. Opportunities and challenges for a sustainable energy future. *Nature*. 2012;488(7411):294–303.
3. Li C, Xin Y, Gao W, Chen Y. Enabling a robust long-life zinc-iodine flow battery by stabilizing the zinc anode in a halide-rich electrolyte. *Small*. 2025;21(41):Article e08359.
4. Huskinson B, Marshak MP, Suh C, Er S, Gerhardt MR, Galvin CJ, Chen X, Aspuru-Guzik A, Gordon RG, Aziz MJ. A metal-free organic–inorganic aqueous flow battery. *Nature*. 2014;505(7482):195–198.
5. Dunn B, Kamath H, Tarascon JM. Electrical energy storage for the grid: A battery of choices. *Science*. 2011;334(6058):928–935.
6. Lin K, Chen Q, Gerhardt MR, Tong L, Kim SB, Eisenach L, Valle AW, Hardee D, Gordon RG, Aziz MJ, et al. Alkaline quinone flow battery. *Science*. 2015;349(6255):1529–1532.
7. Jin S, Shao Y, Gao X, Chen P, Zheng J, Hong S, Yin J, Joo YL, Archer LA. Designing interphases for practical aqueous zinc flow batteries with high power density and high areal capacity. *Sci Adv*. 2022;8(39):Article eabq4456.
8. Yu Z, Jia X, Gao H, Su R, Wang X, Zhao T, Jiang H. Unlocking interfacial dynamics of porous electrode via vertical-aligned bismuth-nanosheet decorating for vanadium redox flow batteries. *Adv Funct Mater*. 2024;35(17):2420534.
9. Yang W, Zhang R, Lu M, Lin Y, Liang L, Xu Q. Novel flow field design for redox flow battery using algorithmic channel generation and self-adaptive network model and experimental verification. *Chem Eng J*. 2024;499:Article 156346.
10. Huo X, Shi X, Wang Q, Zeng Y, An L. High-voltage pH-decoupling aqueous redox flow batteries for future energy storage. *Curr Opin Electrochem*. 2025;49:Article 101633.
11. Guo J, Pan L, Sun J, Wei D, Dai Q, Xu J, Li Q, Han M, Wei L, Zhao T. Metal-free fabrication of nitrogen-doped vertical graphene on graphite felt electrodes with enhanced reaction kinetics and mass transport for high-performance redox flow batteries. *Adv Energy Mater*. 2024;14(1):2302521.
12. DeBruler C, Hu B, Moss J, Luo J, Liu TL. A sulfonate-functionalized viologen enabling neutral cation exchange, aqueous organic redox flow batteries toward renewable energy storage. *ACS Energy Lett*. 2018;3(3):663–668.
13. Meng F, Dong X, Wu H, Wu Z, Dou H, Zhang X. Crystalline hydrogen enhanced dual-acid quasi-solid-state proton battery. *Adv Funct Mater*. 2025;35(23):2422079.
14. Na Z, Yao R, Yan Q, Sun X, Huang G. General growth of carbon nanotubes for cerium redox reactions in high-efficiency redox flow batteries. *Research*. 2019;2019:Article 3616178.
15. Parker JF, Pala IR, Machler M, Burz MF, Long JW, Rolison DR. Rechargeable nickel–3D zinc batteries: An energy-dense, safer alternative to lithium-ion. *Science*. 2017;356(6336):415–418.
16. Ma L, Schroeder MA, Borodin O, Pollard TP, Ding MS, Wang C, Xu K. Realizing high zinc reversibility in rechargeable batteries. *Nat Energy*. 2020;5(10):743–749.
17. Gong K, Ma X, Conforti KM, Kuttler KJ, Grunewald JB, Yeager KL, Bazant MZ, Gu S, Yan Y. A zinc–iron redox-flow battery under $100 per kW h of system capital cost. *Energy Environ Sci*. 2015;8(10):2941–2945.
18. Yuan Z, Liu X, Xu W, Duan Y, Zhang H, Li X. Negatively charged nanoporous membrane for a dendrite-free alkaline zinc-based flow battery with long cycle life. *Nat Commun*. 2018;9(1):3731.

19. Zhang L, Ding H, Gao H, Gong J, Guo H, Zhang S, Yu Y, He G, Deng T, Parkin IP, et al. An integrated design for high-energy, durable zinc–iodine batteries with ultra-high recycling efficiency. *Energy Environ Sci*. 2025;18(5):2462–2473.
20. Zhu W, Lei Z, Wu P. Multi-stage collaborative design of hierarchical twisted hydrogel electrolytes for aqueous zinc-ion batteries with high capacity, ultralong stability, and mechanical robustness. *Energy Environ Sci*. 2025;18(8):3647–3558.
21. Xu J, He M, Jin H, Xie X, Ye C, Ding M, Cheng Y, Bai F, Zhang J, Lou X, et al. Nano-sponge in concomitant swelling membrane for redox flow batteries with high operational stability. *Adv Energy Mater*. 2025;15(37):Article e02374.
22. Tan R, Wang A, Ye C, Li J, Liu D, Darwich B, Petit L, Fan Z, Wong T, Alvarez-Fernandez A, et al. Thin film composite membranes with regulated crossover and water migration for long-life aqueous redox flow batteries. *Adv Sci*. 2023;10(20):2206888.
23. Zhao Y, Wang X, Jia C, Ding M. Regulating the solvation structure of $Zn^{2+}$ via glycine enables a long-cycling neutral zinc-ferricyanide flow battery. *J Colloid Interface Sci*. 2024;673:496–503.
24. Wang J, Liu Z, Xu Z, Ding M, Lu B, Jia C, Zhou G. Redox-mediated lithium recovery from spent $LiFePO_4$ stabilizes ferricyanide catholyte for durable zinc-ferricyanide flow batteries. *Angew Chem Int Ed*. 2025;64(24):Article e202503109.
25. Li X, Yao Y, Liu C, Jia X, Jian J, Guo B, Lu S, Qin W, Wang Q, Wu X. Lithium ferrocyanide catholyte for high-energy and low-cost aqueous redox flow batteries. *Angew Chem Int Ed*. 2023;62(25):Article e202304667.
26. Wang G, Zou H, Xu Z, Tang A, Zhong F, Zhu X, Qin C, Ding M, You W, Jia C. Unlocking the solubility limit of ferrocyanide for high energy density redox flow batteries. *Mater Today Energy*. 2022;28:Article 101061.
27. Wang C, Gao G, Su Y, Xie J, He D, Wang X, Wang Y, Wang Y. High-voltage and dendrite-free zinc-iodine flow battery. *Nat Commun*. 2024;15(1):6234.
28. Amini K, Shocron AN, Suss ME, Aziz MJ. Pathways to high-power-density redox flow batteries. *ACS Energy Lett*. 2023;8(8):3526–3535.
29. Jiang J, Chen Y, Li Y, Ju Z, Yang J, Kumar S, Tee SY, Yu G, Seh ZW. Regulating $Zn^{2+}$ solvation structure in eutectic electrolytes for rechargeable zinc batteries. *Matter*. 2025;8(2):Article 101917.
30. Qiu M, Sun P, Liang Y, Chen J, Wang Z, Mai W. Tailoring tetrahedral and pair-correlation entropies of glass-forming liquids for energy storage applications at ultralow temperatures. *Nat Commun*. 2024;15(1):10420.
31. Ai F, Wang Z, Lai NC, Zou Q, Liang Z, Lu YC. Heteropoly acid negolytes for high-power-density aqueous redox flow batteries at low temperatures. *Nat Energy*. 2022;7(5):417–426.
32. Jin C, Yang C, Xie L, Mi H, Yin H, Xu B, Guo F, Qiu J. Regulating water activity and solvation structure via zwitterion-enhanced polymer electrolyte for long-life Zn-ion hybrid capacitors with low-temperature applicability. *Adv Energy Mater*. 2024;15(4):2402843.
33. Yu Y, Zhang Q, Zhang P, Jia X, Song H, Zhong S, Liu J. Massively reconstructing hydrogen bonding network and coordination structure enabled by a natural multifunctional co-solvent for practical aqueous Zn-ion batteries. *Adv Sci*. 2024;11(22):Article e2400336.
34. Lu X, Liu Z, Amardeep A, Wu Z, Tao L, Qu K, Sun H, Liu Y, Liu J. Ultra-stable zinc metal anodes at −20 °C through eutectic solvation sheath in chlorine-functionalized eutectic electrolytes with 1,3-dioxolane. *Angew Chem Int Ed*. 2023;62(33):Article e202307475.
35. Chang N, Li T, Li R, Wang S, Yin Y, Zhang H, Li X. An aqueous hybrid electrolyte for low-temperature zinc-based energy storage devices. *Energy Environ Sci*. 2020;13(10):3527–3535.
36. Luo J, Hu B, Debruler C, Bi Y, Zhao Y, Yuan B, Hu M, Wu W, Liu TL. Unprecedented capacity and stability of ammonium ferrocyanide catholyte in pH neutral aqueous redox flow batteries. *Joule*. 2019;3(1):149–163.
37. Zheng L, Zhu C, Zhang Z, Fu X, Ruan H, Xiao Y, Wu Z, Wan F, Guo X. Insights into the effects of organic electrolyte additives on proton insertion for low-temperature aqueous zinc batteries. *ACS Appl Mater Interfaces*. 2025;17(24):35446–35456.
38. Wang F, Blanc LE, Li Q, Faraone A, Ji X, Chen-Mayer HH, Paul RL, Dura JA, Hu E, Xu K, et al. Quantifying and suppressing proton intercalation to enable high-voltage Zn-ion batteries. *Adv Energy Mater*. 2021;11(41):2102016.
39. Zhang Y, Shen S, Kang Z, Gao N, Yin D, Zhao L, Wen B, Deng T, Xi K, Su Y, et al. Densely packed spherical zinc deposition by a cation buffer strategy led to high-rate alkaline zinc batteries with lean electrolytes. *Energy Environ Sci*. 2025;18(8):3668–3679.
40. Geng L, Meng J, Wang X, Wu W, Han K, Huang M, Han C, Wu L, Li J, Zhou L, et al. Organic-solvent-free primary solvation shell for low-temperature aqueous zinc batteries. *Chem*. 2024;11(2):Article 102302.
41. Huang J, Guo X, Lin X, Zhu Y, Zhang B. Hybrid aqueous/organic electrolytes enable the high-performance Zn-ion batteries. *Research*. 2019;2019:2635310.
42. Xie C, Yang Z, Zhang Q, Ji H, Li Y, Wu T, Li W, Wu P, Wang H. Designing zinc deposition substrate with fully preferred orientation to elude the interfacial inhomogeneous dendrite growth. *Research*. 2022;2022:9841343.
43. Zhi L, Liao C, Xu P, Li G, Yuan Z, Li X. Zinc-ferricyanide flow batteries operating stably under −10 °C. *Angew Chem Int Ed*. 2024;63(51):Article e202412559.
44. Zhi L, Liao C, Xu P, Sun F, Fan F, Li G, Yuan Z, Li X. New alkalescent electrolyte chemistry for zinc-ferricyanide flow battery. *Angew Chem Int Ed*. 2024;63(28):Article e202403607.
45. Chen M, Song W, Lin W, Feng Z. Ice nucleation in supercooled water under shear. *Chem Eng Sci*. 2024;300:Article 120674.
46. Inada T, Tomita H, Koyama T. Ice nucleation in water droplets on glass surfaces: From micro- to macro-scale. *Int J Refrig*. 2014;40:294–301.
47. Qiu M, Sun P, Han K, Pang Z, Du J, Li J, Chen J, Wang Z, Mai W. Tailoring water structure with high-tetrahedral-entropy for antifreezing electrolytes and energy storage at −80 °C. *Nat Commun*. 2023;14(1):601.
48. Zhu C, He X, Shi Y, Wang Z, Hao B, Chen W, Yang H, Zhang L, Ji H, Liu J, et al. Strong replaces weak: Design of H-bond interactions enables cryogenic aqueous Zn metal batteries. *ACS Nano*. 2023;17(21):21614.
49. Guo X, Hong H, Li Q, Zhu J, Wu Z, Wang Y, Yang S, Huang Z, Huang Y, Li N, et al. Dual robust electrode-electrolyte interfaces enabled by fluorinated electrolyte for high-performance zinc metal batteries. *Matter*. 2024;7(11):4014–4030.
50. Chen Y, Yin B, Zeng Y, Wang H, Xie B, Luan D, Hu Y, Lou X. Ion-dipole-interaction-manipulated bilateral interface

chemistry for deep rechargeability and high redox activity of Zn-organic batteries. *Chem*. 2025;11(6):Article 102411.
51. Yang J-L, Yang P, Xiao T, Fan H. Designing single-ion conductive electrolytes for aqueous zinc batteries. *Matter*. 2024;7(6):1928–1949.
52. Zhang Y, Hu Z, Bi Y, Sun L, Tian S, Sun H, Li K, Liu W, Liu W, Huang G, et al. Epitaxial Zn (002) growth directed by Cu (111): A dual-layer strategy toward stable and reversible Zn metal anodes. *Energy Storage Mater*. 2025;79:Article 104366.
53. Yu D, Zhi L, Zhang F, Song Y, Wang Q, Yuan Z, Li X. Scalable alkaline zinc-iron/nickel hybrid flow battery with energy density up to 200 Wh $L^{-1}$. *Adv Mater*. 2023;35(7):2209390.
54. Ling R, Zhu Z, Peng K, Fang J, Zou W, Li Q, Liu Y, Zhu Q, Lin N, Xu T, et al. Dual-function electrolyte additive design for long life alkaline zinc flow batteries. *Adv Mater*. 2024;36(28):2404834.
55. Yang X, Wei Z, Hu H, Hong H, Wang Y, Zhu J, Li P, Wang T, Fan J, Zhi C. Lewis acid-driven weak electrostatic interaction of polybenzimidazole-based membrane for alkaline zinc-iron redox flow batteries. *Adv Mater*. 2025;37(45):Article e10023.
56. Wang S, Li T, Yuan C, Zhu J, Li P, Zhang S, Wei Z, Wang Y, Li X, Zhi C. Realizing an anolyte utilization rate of 99% in low-cost zinc-based flow batteries by rejuvenating dead zinc. *Energy Environ Sci*. 2024;17(19):7155.
57. Cao X, Wang X, Xue X. A low-cost and green zinc-iron battery achieved by ethaline deep eutectic solvent. *ChemSusChem*. 2024;18(5):Article e202401604.
58. Hu J, Yue M, Zhang H, Yuan Z, Li X. A boron nitride nanosheets composite membrane for a long-life zinc-based flow battery. *Angew Chem Int Ed*. 2020;59(17):6715–6719.
59. Chen Z, Li T, Xie C, Li X. A neutral zinc–iron flow battery with long lifespan and high power density. *ACS Energy Lett*. 2024;9(7):3426–3432.
60. Cai Y, Zhang H, Wang T, Xi S, Song Y, Rong S, Ma J, Han Z, Low C, Wang Q, et al. Directional regulation on single-molecule redox-targeting reaction in neutral zinc-iron flow batteries. *Joule*. 2025;9(1):Article 101768.